We are IntechOpen,
the world's leading publisher of
Open Access books
Built by scientists, for scientists

6,900
Open access books available

185,000
International authors and editors

200M
Downloads

154
Countries delivered to

Our authors are among the

TOP 1%
most cited scientists

12.2%
Contributors from top 500 universities

CLARIVATE ANALYTICS
BOOK CITATION INDEX
INDEXED

WEB OF SCIENCE™

Selection of our books indexed in the Book Citation Index
in Web of Science™ Core Collection (BKCI)

Interested in publishing with us?
Contact book.department@intechopen.com

Numbers displayed above are based on latest data collected.
For more information visit www.intechopen.com

Ray-Thermal-Structural Coupled Analysis of Parabolic Trough Solar Collector System

Yong Shuai, Fu-Qiang Wang, Xin-Lin Xia and He-Ping Tan
School of Energy Science and Engineering, Harbin Institute of Technology,
No. 92, West Dazhi Street, Harbin 150001
P. R. China

1. Introduction

An effective approach to sustainable energy is the utilization of solar energy. The parabolic trough collector with central receiver is one of the most suitable systems for solar power generation. A type of concentrating solar collector that uses U-shaped troughs to concentrate sunlight onto a receiver tube, containing a working fluid such as water or oil, which is positioned along the focal line of the trough. Sometimes a transparent glass tube envelops the receiver tube to reduce heat loss. Parabolic troughs often use single-axis or dual-axis tracking. Temperatures at the receiver can reach 400°C. The heated working fluid may be used for medium temperature space or process heat, or to operate a steam turbine for power or electricity generation. As designed to operate with concentrated heat fluxes, the receiver will be subjected to the high thermal stresses which may cause the failure of receivers.

The thermal stress of receiver or tube heat exchangers has drawn many researchers' attention. Numerous studies have been carried out to investigate the temperature distributions and thermal stress fields of receiver or tube heat exchangers. A numerical analysis had been conducted by Chen [1] to study the effect on temperature distributions of using porous material for the receiver. Experiments were conducted by Fend [2] to research the temperature distributions on the volumetric receivers used two novel porous materials. A finite element analysis was conducted by Islamoglu [3] to study the temperature distribution and the thermal stress fields on the tube heat exchanger using the SiC material. To reduce the thermal stresses, Agrafiotis [4] employed porous monolithic multi-channeled SiC honeycombs as the material for an open volumetric receiver. Low cycle fatigue test of the receiver materials was conducted at different temperatures by Lata et al. [5], the results showed that the high nickel alloys had excellent thermo-mechanical properties compared to the austenitic stainless steel. Almanza and Flores [6, 7] proposed a bimetallic Cu-Fe type receiver, and the experimental test results showed that, when operated at low pressure, the bimetallic Cu-Fe type receiver had a lower thermal gradient and less thermal stress strain than the steel receiver. In Steven's study [8], the receiver is divided into 16 sections, and the average solar radiation heat flux of each section is calculated. The average heat flux is used as boundary condition for each corresponding section in the thermal analysis model. This method is fairly straightforward and simple, but the deviations generated during the heat flux transformation process are enormous.

In this section, the conjugate heat transfer and thermal stress analyses of tube receiver are carried out with concentrated solar irradiation heat flux conditions. A ray-thermal-structural sequential coupled method is adopted to obtain the concentrated heat flux distributions, temperature distributions and thermal stress fields of tube receiver. The concentrated solar irradiation heat flux distribution converged by solar parabolic collector is obtained by Monte-Carlo ray tracing method and used as boundary conditions for CFD analysis by fitting function method. Steady state conjugate heat transfer is performed to calculate temperature field using CFD system and the resulted temperature defined at the nodes of CFD mesh is interpolated as input data to the nodes in the thermal-stress analysis mesh.

2. Methodology

2.1 Radiative flux calculation

Monte Carlo (MC) method is a statistical simulation method for radiative transfer, which can be performed by tracing a finite number of energy rays through their transport histories. What a ray does at each interaction and where it goes is then determined by the probability for each process (refraction, reflection, absorption, diffraction, scatter and emission). Modest [9] and Siegel [10] have described the MC simulation in detail, respectively.

A Monte-Carlo ray tracing computational code [11], which is based on the radiative exchange factor (REF) theory, is developed to predict the heat flux distribution on the bottom surface of the tube receiver. The REF $RD_{i,j}$ is defined as the fraction of the emissive power absorbed by the jth element in the overall power emitted by the ith element. The jth element can absorb the emissive power within the system by the means of direct radiation, direct reflection and multiple reflections. The values of the $RD_{i,j}$ are determined by both the geometry and radiative characteristics of the computational elements.

The REF within the spectral band $\Delta\lambda_k$ ($k = 1, 2, ..., M_b$) can be expressed as follows:

$$RD_{i,j,\Delta\lambda_k} = N_{i,j} / N_i \tag{1}$$

where N_i is the total bundles emitted by the i th element, $N_{i,j}$ is the bundles absorbed by the j th element, and M_b is the total spectral bands of the wavelength-dependent radiation characteristics of the surface. As shown in Fig. 1, the concentrated heat flux distribution on the bottom surface of the tube receiver can be expressed as follows:

$$q_{r,j} = \frac{A_i}{A_j} \sum_{k=1}^{M_b} RD_{i,j,\Delta\lambda_k} E_{sun,\Delta\lambda_k} \tag{2}$$

where $q_{r,j}$ is the heat flux of the j th surface element of the tube receiver, A_i is the area of the imaginary emission surface, A_j is the area of the j th surface element of the tube receiver, and $E_{sun,\Delta\lambda_k}$ is the sun average spectral irradiance within the spectral band $\Delta\lambda_k$.

2.2 Thermal stress analyses

In order to analyze thermal stress, a ray-thermal-structural coupled method [12] is adopted to obtain temperature distribution and thermal stress field of tube receiver in the parabolic trough solar thermal collector system. At the first step, the concentrated solar radiation heat flux distribution q_c on the bottom half periphery of tube receiver, which is used as the input
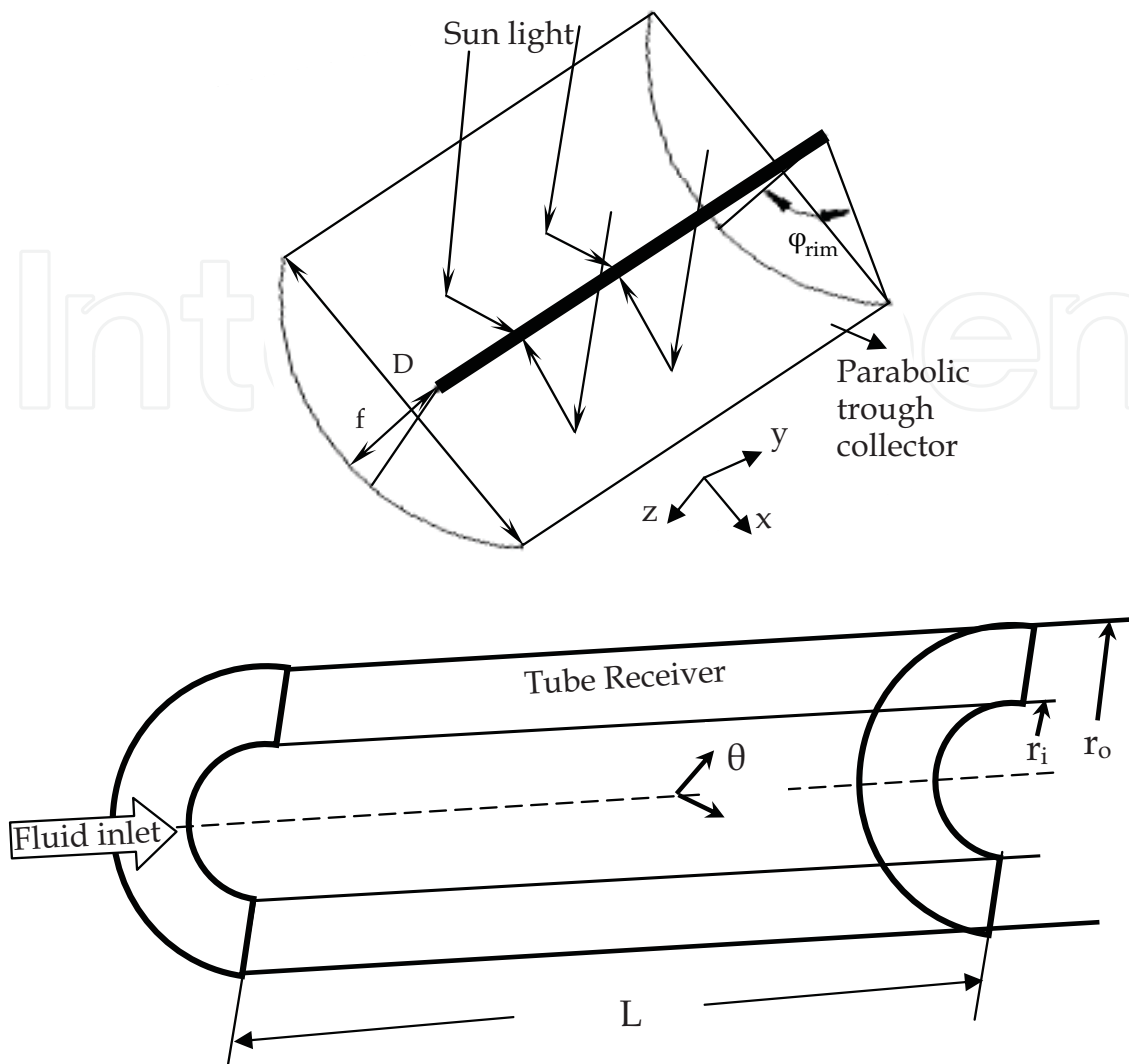
Fig. 1. Schematic diagram of the parabolic collector and receiver

data for the CFD analyses, will be calculated by the solar concentration system program with the Monte-Carlo ray tracing method. The thermal model proposed for the solar parabolic collector with tube receiver system is illustrated in Fig. 1. The geometrical parameters of the parabolic trough collector and tube receiver for this study are illustrated in Table 1. As seen from this table, the transmissivity of the glass envelop is highly close to 1, and the thickness of glass envelop is very thin, therefore, the values and distribution of heat flux are impacted very slightly when passing through the glass envelop. Therefore, this investigation doesn't consider the impact of glass envelop. During the heat flux distribution calculation process, the external cylinder surface of tube receiver will be discretized to 300 nodes along the circumference and 300 nodes along the tube length direction. Therefore, the solar concentration system program will obtain 300 × 300 heat flux values on the discrete nodes. No optical errors or tracking errors were considered for the solar concentration system program, and the calculation conditions are: the non-parallelism angle of sunlight is 16' and the solar radiation flux is 1,000 W/m².

At the second step, the concentrated heat flux distribution calculated by the Monte-Carlo ray tracing method will be employed as input data for the CFD analyses by means of using the boundary condition function in Ansys software. In this study, the fitting function

Parabolic trough collector and tube receiver	Value
Focal length of parabolic trough collector	2,000 (mm)
Length of parabolic trough collector	2,000 (mm)
Opening radius of parabolic trough collector	500 (mm)
Height of parabolic trough collector	1500 (mm)
Outer diameter of tube receiver (r_{out})	70 (mm)
Inner diameter of tube receiver (r_{in})	60 (mm)
Glass cover diameter	100 (mm)
Length of tube receiver	2,000 (mm)
Reflectivity of parabolic trough collector	0.95
Absorptivity of tube receiver	0.9
Transmissivity	0.965

Table 1. Geometrical parameters of the parabolic trough collector and tube receiver

method is introduced for the calculated heat flux distribution transformation from the Monte-Carlo ray tracing model to the CFD analysis model. The radiation heat flux distribution calculated by the Monte-Carlo ray tracing method along the bottom half periphery of tube receiver will be divided in to several sections, and the heat flux distribution of each section will be fitted by a polynomial regression function with highly fitted precision. The calculated heat flux distribution on the bottom half periphery of tube receiver is shown in Fig.2 and Fig. 3. Six polynomial regression functions are employed as the fitted functions and illustrated as follows:

$$\begin{cases} q = 12 & x \in [-35, \ -17.82] \\ q = 13740.23 + 770556.99 \times x & x \in [-17.82, \ -16.54] \\ q = 43418.96 + 2.57 \times x & x \in [-16.54, \ 0] \\ q = 43418.96 - 2.57 \times x & x \in [0, \ 16.54] \\ q = 13740.23 - 770556.99 \times x & x \in [16.54, \ 17.82] \\ q = 12 & x \in [17.82, \ 35] \end{cases} \tag{3}$$

The six fitted function curves are also drawn in Fig. 3. As seen from this figure, the fitted function curves can match the calculated heat flux distribution well with high precision.

At the third step, the CFD analyses will obtain the temperature distributions. Thermal oil (Syltherm 800) and stainless steel are used as the heat transfer fluid and the material of tube receiver respectively. The thermal-physical properties of the thermal oil and four different materials are presented in Table 2. The boundary conditions applied on the tube receivers are illustrated as follows:

- The flow has a uniform velocity u at atmosphere temperature at the tube receiver inlet;
- The top half periphery of tube receiver is subjected to a uniform heat flux distribution which is the sun average radiation in the air (the value is 1,000 W/m²);
- The bottom half periphery of tube receiver is subjected to the concentrated heat flux distribution calculated by the Monte-Carlo ray tracing method which is fitted by six polynomial regression functions;

• Zero pressure gradient condition is employed across the fluid outlet boundary.

At the forth step, the finite element analysis (FEA) will obtain the Von-Mises thermal stress fields, which is a synthesis stress of radial stress, axial stress and circumferential stress. According to the Von-Mises stress theory [13], the formulation to calculate the Von-Mises stress σ_{eff} is:

$$\sigma_{eff} = \sqrt{\sigma_r^2 + \sigma_z^2 + \sigma_\theta^2 - (\sigma_r\sigma_z + \sigma_r\sigma_\theta + \sigma_\theta\sigma_z)} \tag{4}$$

where σ_r, σ_z, σ_θ are the radial stress, axial stress and circumferential stress respectively. The resulted temperature fields defined at the nodes of CFD analysis meshes are interpolated as input data to the nodes of the thermal stress analysis meshes. This simulation approach is fairly straightforward and has been adopted by many investigators.

Property	Fluid	Tube receiver			
	Thermal Oil	Stainless steel	Aluminum	Copper	SiC
Density (kg m^{-3})	938	7900	2698	8930	3210
Specific Heat (J kg^{-1} K^{-1})	1970	500	879	386	2540
Viscosity (10^{-6} Pa s)	15.3	48	247	384	42
Thermal Conductivity (W m^{-1} K^{-1})	`0.118	220	70	128	427
Poisson Ratio	—	0.25	0.32	0.31	0.17
Young's Modulus (Gpa)	—	17.2	23.6	17.1	4.8
Thermal expansion coefficient (10^{-6} K^{-1})	—	450	130	270	400

Table 2. Thermal-physical properties of heat transfer fluid and tube receiver
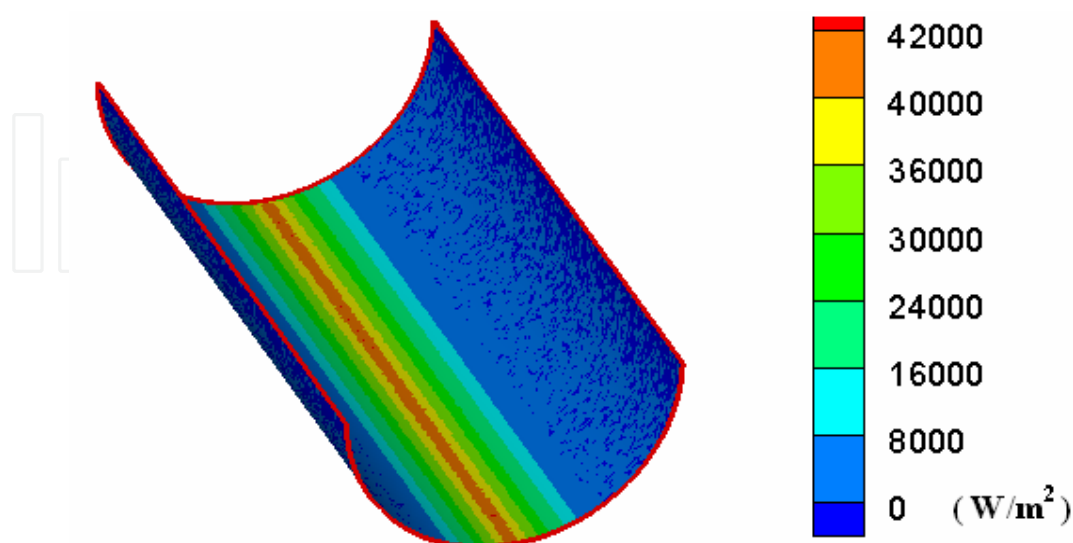
Fig. 2. Concentrated solar irradiation heat flux distribution on the bottom surface of tube receiver.
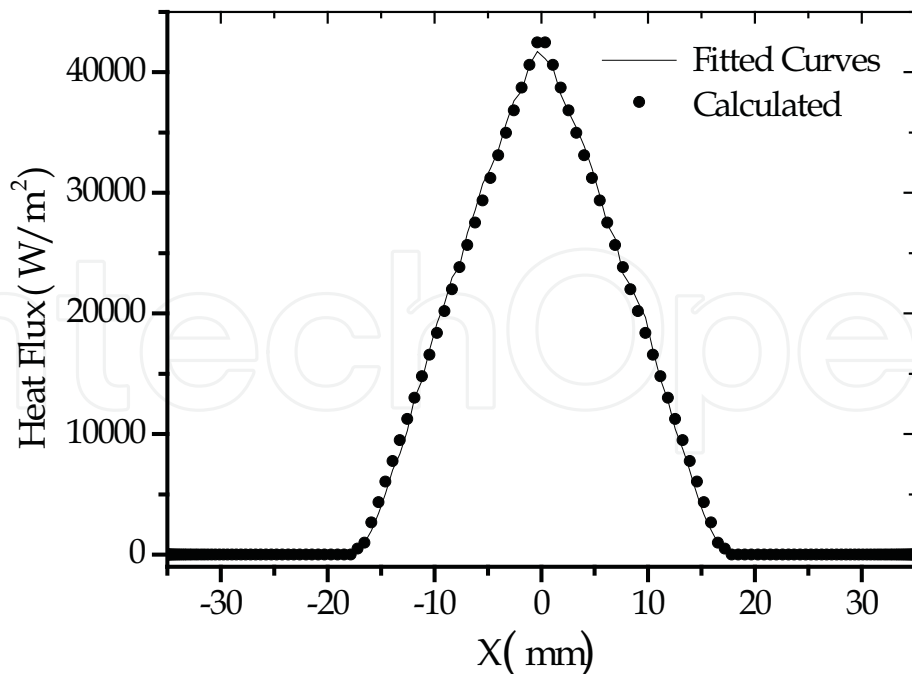
Fig. 3. Calculated heat flux distribution on the bottom half periphery of tube receiver and the fitted function curves.

The validation of this simulation approach has been described in [14], and the comparison between the simulation results and the experimentations reveals a high level of compliance. The detail of the computational meshes is presented in Fig. 4. All of the meshes are generated with O-grid method by Ansys Workbench software. In this study, a finer solid part mesh is used in thermal stress analysis to produce a reasonably accurate degree of freedom solution. There are 24,000 mesh elements in solid part and 62,000 mesh elements in fluid part for the CFD analysis and 123,280 mesh elements in the finer solid part mesh for thermal stress analysis.

3. Ray-thermal-structural analysis of concentric tube receiver

3.1 Comparisons between uniform and concentrated heat flux conditions

The temperature distribution and thermal stress field of the tube receiver with uniform and concentrated solar irradiation heat flux conditions are obtained. Fig. 5 and Fig. 6 show the temperature contours on the outlet surface and outer surface of the tube receiver respectively both for uniform and concentrated solar irradiation heat flux conditions. The maximal temperature for concentrated solar irradiation heat flux condition is 21 K higher than the maximal temperature for uniform heat flux condition. For concentrated solar irradiation heat flux condition, there are five temperature contour sections at the outlet surface of tube receiver, compared to three temperature contour sections for uniform heat flux conditions. As seen from Fig. 5 and Fig. 6, compared to uniform heat flux condition, the temperature gradients varying with θ and L are higher for concentrated solar irradiation condition, this is caused by the highly concentrated heat flux on bottom surface of tube receiver.

The maximal effective thermal stresses are found at the outlet surface of tube receiver both for uniform and concentrated solar irradiation heat flux conditions. Fig. 7 shows the effective thermal stress contours on the outlet surface. As we expected, due to the higher
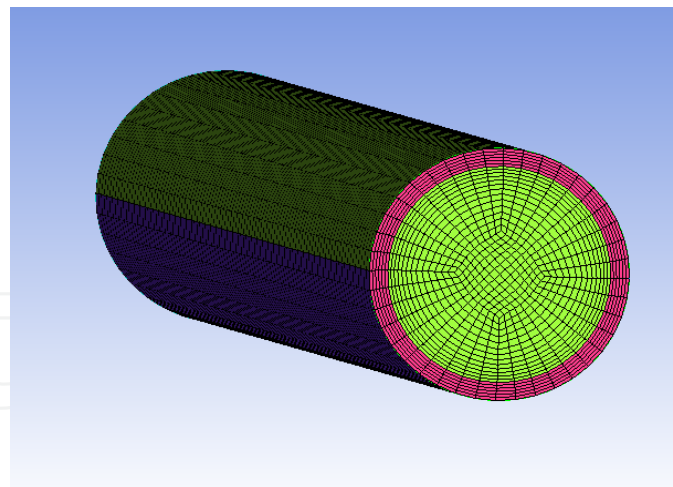
(a) Meshes for CFD analysis
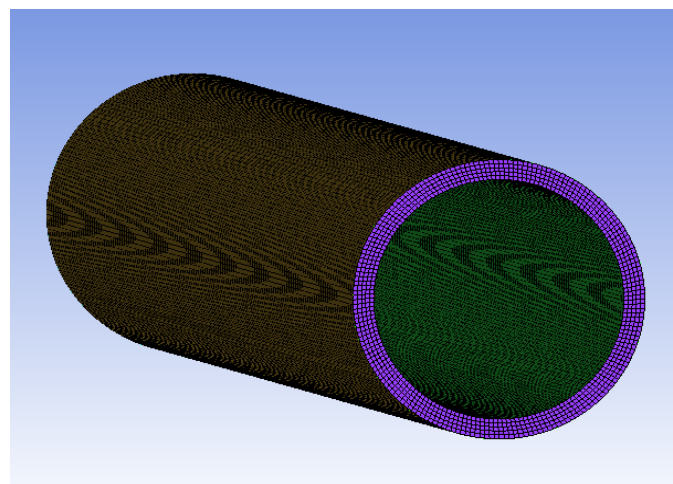

(b) Finer meshes for thermal stress analysis

Fig. 4. Computational meshes for CFD and thermal stress analysis

temperature gradient, the concentrated solar irradiation heat flux condition has a much higher effective thermal stress. The maximal effective thermal stress for concentrated solar irradiation heat flux condition is 73.6 Mpa, which is 4.2 times of the maximal effective thermal stress for uniform heat flux condition.

3.2 Comparisons between different materials

Fig. 8 shows the temperature profiles across the circumference on the tube inner surface at the tube outlet section. Among the four different material conditions, the SiC condition has the highest maximum temperature. Due to the low conductivity of SiC and stainless steel compared with the conductivity of aluminum and copper, as seen from this figure, the temperature gradients of the stainless steel and SiC conditions are much higher than those of the aluminum and copper conditions, which can cause higher thermal stress and reduce the durability of tube receiver.

The numerical result shows that the maximum effective stresses are found at the circumference on the tube inner surface at the tube outlet section at $\theta=270°$ for all the four different material conditions. Fig. 9 shows the effective stress profiles on the tube inner surface along the length direction at $\theta=270°$ for the four different material conditions. As
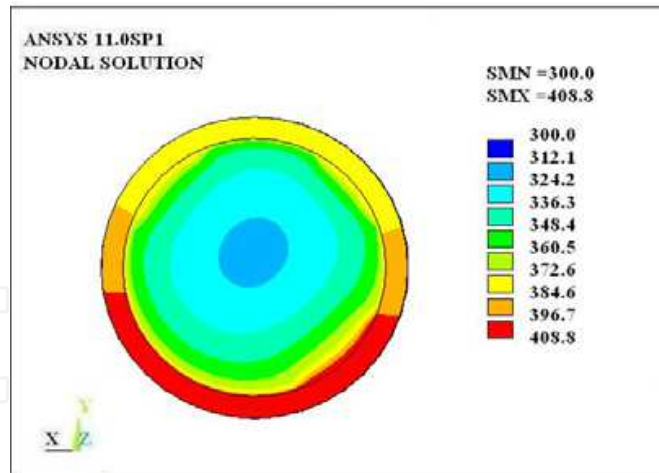
(a) Uniform heat flux
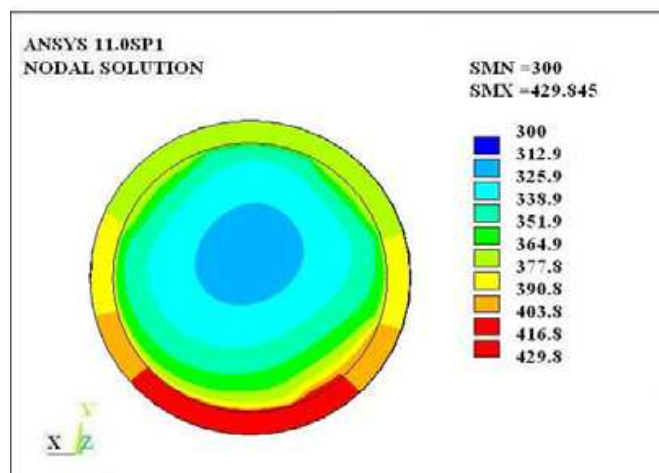
(b) Concentrated solar irradiation heat flux

Fig. 5. Temperature contour on the outlet surface.

seen from the figure, the four profiles have almost the same trend line. At the two free ends of the tube, the effective stress values are much higher than the effective stress values at other positions. This phenomenon may_be caused by the bending movement of the tube receiver at the two free ends due to the outward defection of the tube. From the tube inlet end to z=0.1m, the effective stress values decrease sharply to the lowest of each profile. From z=0.1m to z=1.9m, the tangential stresses of each profile almost keep constant. From z=1.9m to the tube outlet end, the compressive tangential stresses increase sharply to the maximum. Among the four different material conditions, the stainless steel condition has the highest maximum effective stress and the copper condition has the lowest maximum effective stress which is only 4.9 MPa.

In this study, the stress failure ratio F_c ($F_c = \delta_{\text{eff}} / \delta_b \times 100\%$) is introduced to assess the thermal stress level of each material condition. Fig. 10 presents the stress failure ratio profiles on the tube inner surface along the length direction at $\theta = 270^{\circ}$ for the four different material conditions. The copper condition has the lowest stress failure ratio and the stainless steel condition has the highest stress failure ratio which is about 6 times of the copper condition. Therefore, from the standpoint of thermal stress, copper is recommended as the material of tube receiver.
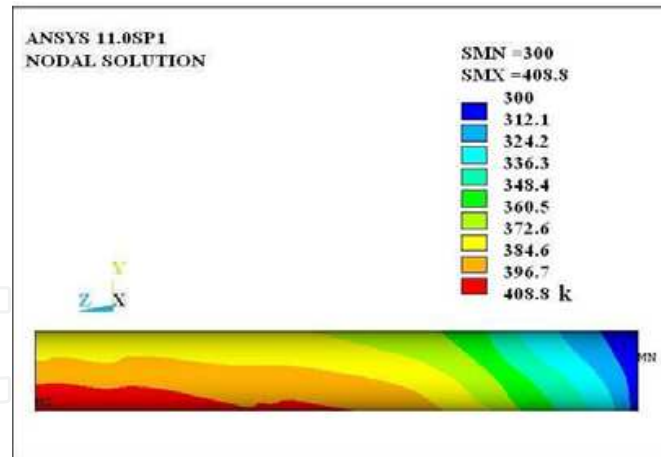
(a) Uniform heat flux
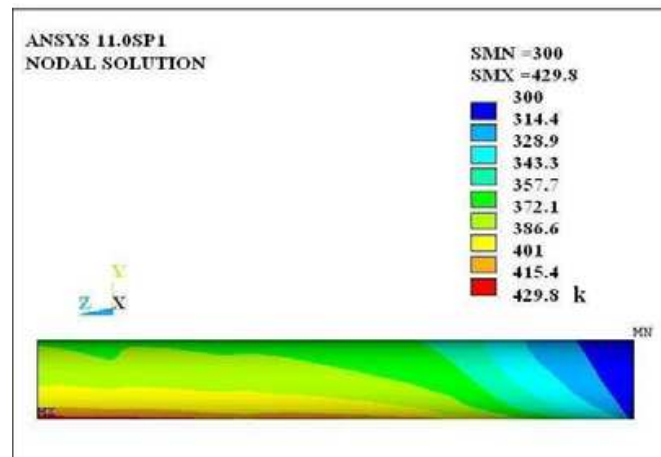
(b) Concentrated solar irradiation heat flux

Fig. 6. Temperature contour on the outer surface.

4. Ray-thermal-structural analysis of eccentric tube receiver

As mentioned in the previous section, the tube receivers are designed to operate under extremely nonuniform heat flux, cyclic weather and cloud transient cycle's conditions, which in turn will produce high temperature gradients and large deflection of tube receiver. The high temperature gradients will generate the large thermal stresses which may cause the failure of tube receiver, and the deflection of tube receiver will induce the rupture of glass envelop which will result in the increase of heat loss. Therefore, it is necessary to seek some new approaches to reduce the thermal stresses and deflection of the tube receiver.

Hitherto, mainly three methods have been proposed to reduce the thermal stresses or deflection of receiver:

• Optimizing the size of tube receivers or operation parameters, such as, employing small diameter tubes; or controlling the fluid flow rate.

• Receivers with homogenous solar radiation heat flux distribution on the surface. Generally, these kinds of receivers are designed using ray tracing methods to obtain the isosurface of solar radiation. At present, the literature survey indicates that the research on receivers with homogenous solar radiation heat flux distribution remains at the theory stage, and a large amount of manufacturing problems wait to solve further.
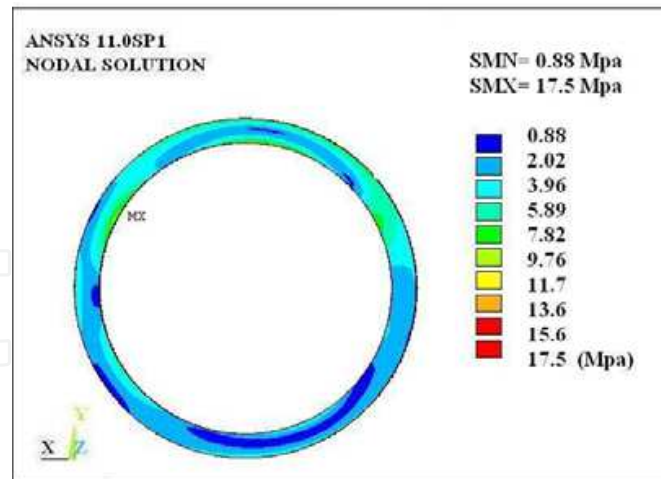
(a) Uniform heat flux
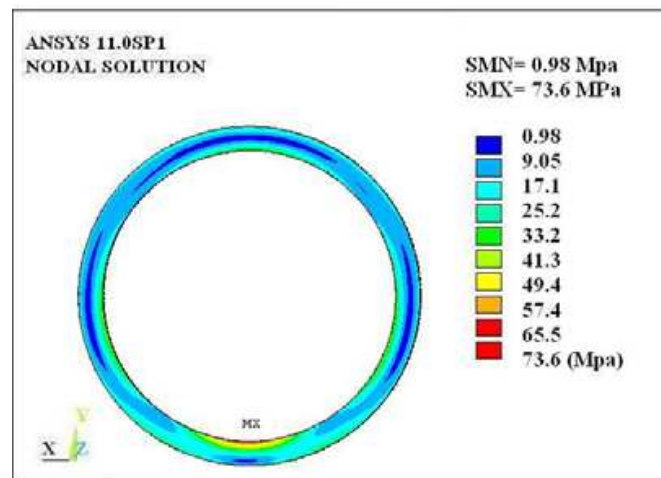

(b) Concentrated solar irradiation heat flux

Fig. 7. Effective stress contour on the outlet surface.

- Compound wall copper-steel receiver. The compound wall receiver is composed of two parts: the internal tube stratified is made of copper to obtain an excellent heat transfer performance to reduce the temperature gradients, and the external tube stratified is made of steel to strengthen the intensity of the tube receiver. The compound wall copper-steel tube receivers have been applied to the Solar Power Plant of the National University of Mexico. Though the compound wall copper-steel receiver can reduce the deflection of tube receiver, it will introduce the contact resistance if the two stratifications can not contact well and the solar radiation absorption efficiency will be affected.

With the aim to reduce the thermal stresses of tube receiver during application, an eccentric tube receiver for the parabolic trough collector system is introduced. The aim of the new-type receiver is to:

- Reducing the thermal stresses effectively
- Without adding the mass of tube receiver
- Easy to manufacture
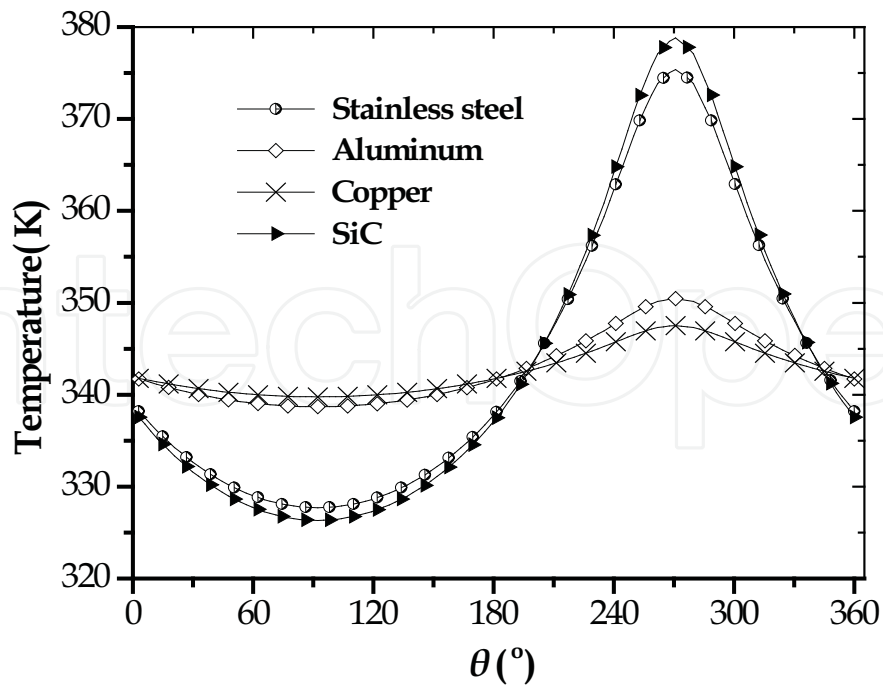
Fig. 8. Temperature profiles across the circumference on the tube inner surface at the tube outlet section
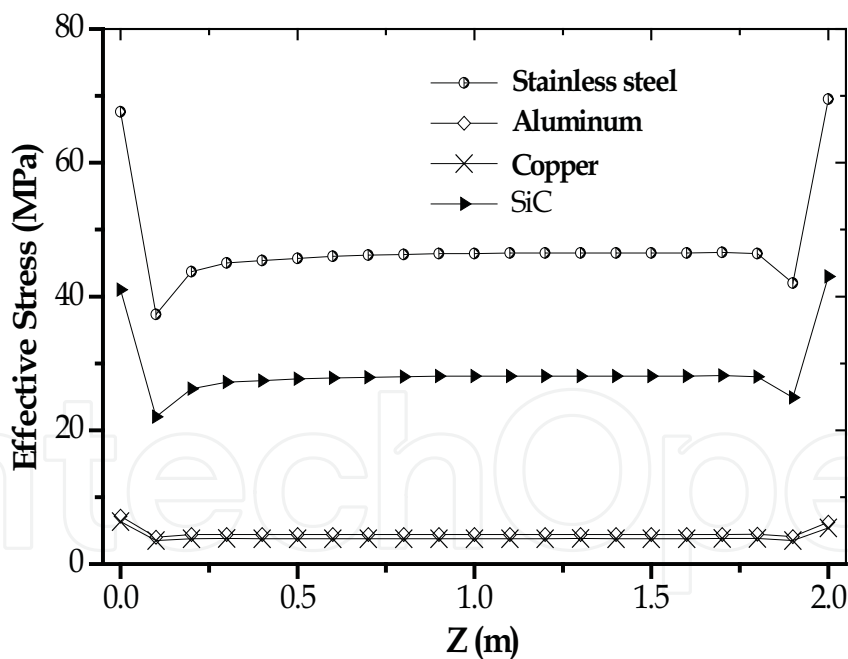
Fig. 9. Effective stress profiles on the tube inner surface along the length direction at θ=270°

4.1 Construction of eccentric tube receiver

To meet the above requirements of the new type receiver, the eccentric tube receiver for parabolic trough collector system is introduced. Fig. 11 shows the diagram of the eccentric tube receiver. The eccentric tube receiver is proposed on the basis of concentric tube receiver. As seen from this figure, the center of internal cylinder surface of concentric tube
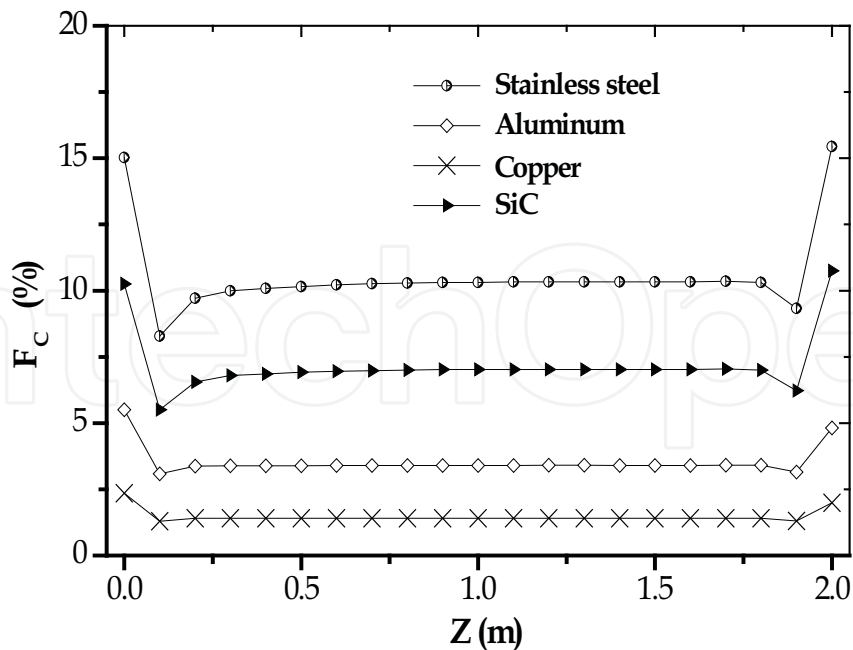
Fig. 10. Stress failure ratio profiles on the tube inner surface along the length direction at $\theta=270°$
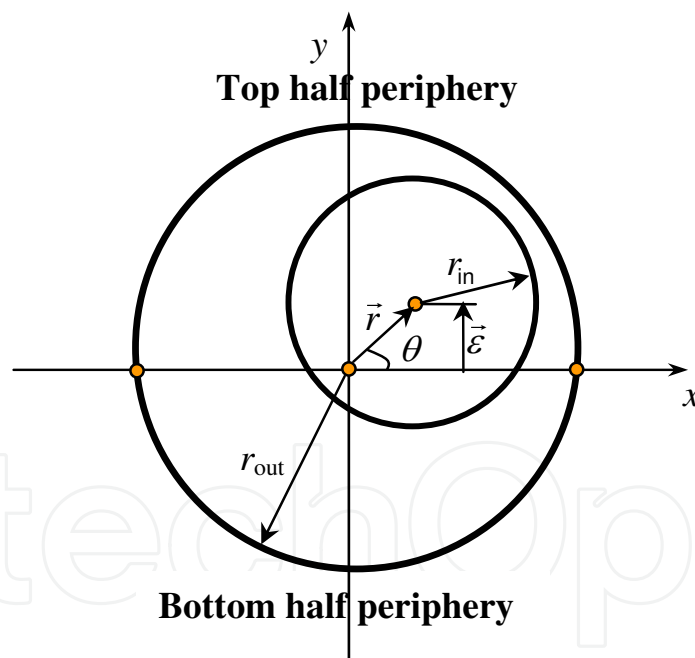
Fig. 11. Schematic diagram of physical domain and coordinate system for the eccentric tube receiver.

receiver is moved upward (or other directions), which is not located at the same coordinate position with the center of external cylinder surface. Therefore, the wall thickness of the bottom half section of tube receiver will increase without adding any mass to the entire tube receiver. With the same boundary conditions for numerical analyses, the increase of wall thickness will not only strengthen the intensity to enhance the resistance of thermal stress,

but also can increase the thermal capacity, which in turn will be benefit to alleviate the extremely nonuniform temperature distribution situation.

As seen from Fig. 11, the origin of coordinate system is placed at the center of the external cylinder surface. In this study, the vector eccentric radius $\vec{r}$ (the origin of coordinate system points to the center of the internal cylinder surface); the vector eccentricity $\vec{\varepsilon}$ (the projection of vector $\vec{r}$ on the y-axis); and the oriented angle θ (the angle between the vector $\vec{r}$ and the x-axis) are introduced to describe the shape of eccentric tube receiver.

4.2 Comparison between the concentric and eccentric tube receiver

The eccentric tube receiver with the center of internal cylinder surface 3 mm moved upward along the y-axis (the magnitude of vector eccentricity $\vec{r}$ is 3 mm, and the oriented angle θ is 90º) is chosen for the comparison research. The temperature distributions and thermal stress fields of eccentric tube receiver are compared with those of concentric tube receiver under the same boundary conditions and material physical properties.

Fig. 12 shows the temperature distributions along the internal circumference at the outlet section for both the concentric and eccentric tube receivers. As seen from this figure, the concentric tube receiver has a higher value of peak temperature which is about 5 ºC higher than that of eccentric tube receiver. Along the bottom half internal circumference (the θ is between 180º and 360º) where the peak temperatures of both the concentric and eccentric tube receivers are found, the temperature gradients of concentric tube receiver are higher than those of eccentric tube receiver which can lead to the higher thermal stresses, the cause of this phenomenon should be attributed to the thermal capacity increase on the bottom section of tube receiver due to the wall thickness increase on this section.

The thermal stress fields along the internal circumference at the outlet section for both the concentric and eccentric tube receivers are presented in Fig. 13. The peak thermal stress
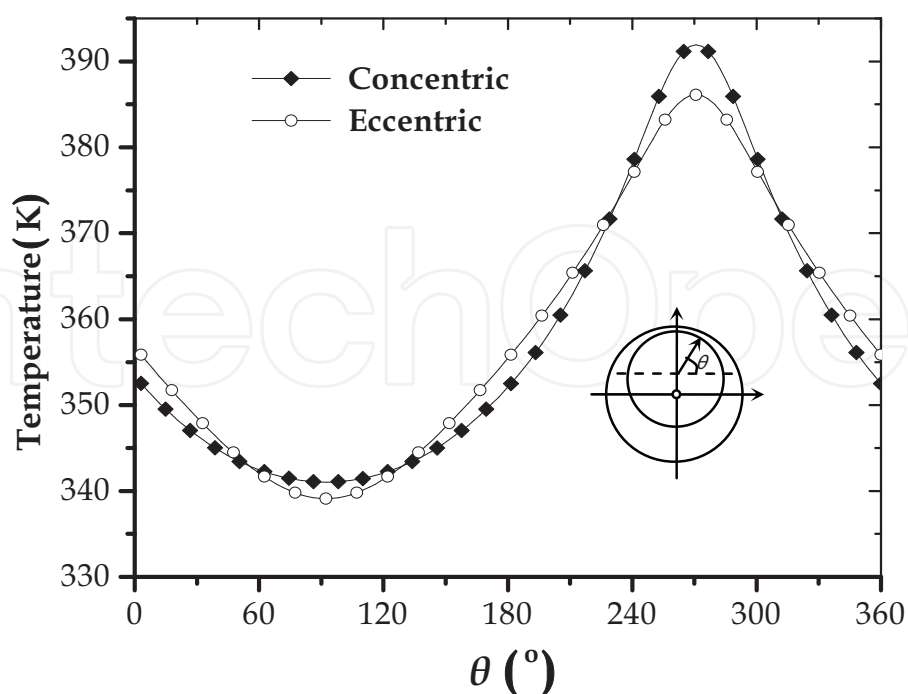

Fig. 12. Temperature profiles along the internal circumference at the outlet section for both the concentric and eccentric tube receivers.
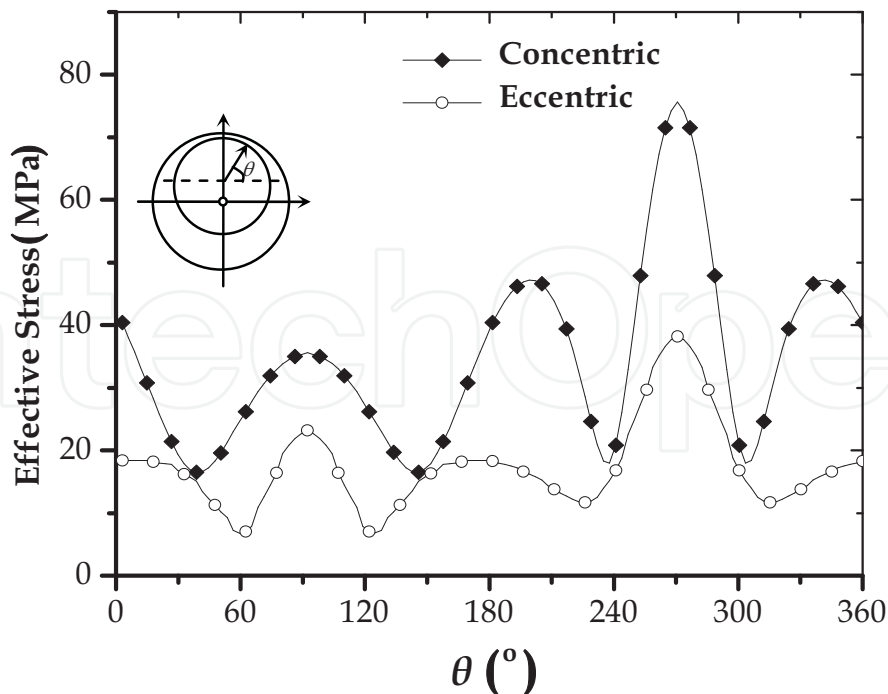
Fig. 13. Thermal stress profiles along the internal circumference at the outlet section for both the concentric and eccentric tube receivers.

values of the two profiles are both found at θ=270° where the peak temperature values are also located at. Attributed to the lower temperature gradients and intensity strengthen on the bottom half section of tube receiver, the peak thermal stress value of the eccentric tube receiver which is only 38.2 MPa is much lower compared to that of the concentric tube receiver which is 71.5 MPa. Therefore, adopting eccentric tube receiver as the tube receiver for parabolic trough collector system can reduce the thermal stresses effectively up to 46.6%, which means the eccentric tube receiver can meet the requirements of the new type receiver.

5. Conclusions

The ray-thermal-structural sequential coupled method is adopted to obtain the concentrated heat flux distributions, temperature distributions and thermal stress fields of both the eccentric and concentric tube receivers. Aiming at reducing the thermal stresses of tube receiver, the eccentric tube receiver is introduced in this investigation. The following conclusions are drawn.
1. For concentrated solar irradiation condition, the tube receiver has a higher temperature gradients and a much higher effective thermal stress.
2. The radial stresses are very small both for uniform and concentrated heat flux distribution conditions due to the little temperature difference between the inner and outer surface of tube receiver. The maximal axial stresses are found at the outer surface of tube receiver both for uniform and concentrated solar irradiation heat flux conditions. The axial stress has more impact on thermal stress compared to radial stresses.
3. The temperature gradients and effective stresses of the stainless steel and SiC conditions are significantly higher than the temperature gradients and effective stresses

of the aluminum and copper conditions. The stainless steel condition has the highest stress failure ratio and the copper condition has the lowest stress failure ratio.

4. Adopting eccentric tube as the tube receiver for parabolic trough collector system can reduce the thermal stress effectively up to 46.6%. The oriented angle has a big impact on the thermal stresses of eccentric tube receiver. The thermal stress reduction of tube receiver only occurs when the oriented angle is between 90° and 180°.

6. Acknowledgements

7. References

C.F. Chen, C.H. Lin, H.T. Jan, Y.L. Yang, Design of a solar collector combining paraboloidal and hyperbolic mirrors using ray tracing method, Opt. Communication 282 (2009) 360-366.

T. Fend, R.P. Paal, O. Reutter, J. Bauer, B. Hoffschmidt, Two novel high-porosity materials as volumetric receivers for concentrated solar radiation, Sol. Energy Mater. Sol. Cells 84 (2004) 291-304.

Y.S. Islamoglu, Finite element model for thermal analysis of ceramic heat exchanger tube under axial concentrated solar irradiation convective heat transfer coefficient, Mater. Design 25 (2004) 479–482.

C.C. Agrafiotis, I. Mavroidis, A.G. Konstandopoulos, B. Hoffschmidt, P. Stobbe, M. Romero, V.F. Quero, Evaluation of porous silicon carbide monolithic honeycombs as volumetric receivers/collectors of concentrated solar radiation, Sol. Energy Mater. Sol. Cells 91 (2007) 474-488.

J.M. Lata, M.A. Rodriguez, M.A. Lara, High flux central receivers of molten salts for the new generation of commercial stand-alone solar power plants, ASME J. Sol. Energy Eng. 130 (2008) 0211002/1–0211002/5.

R.F. Almanza. DSG under two-phase and stratified flow in a steel receiver of a parabolic trough collector, ASME J. Sol. Energy Eng. 124 (2002) 140–144.

V.C. Flores, R.F. Almanza, Behavior of compound wall copper-steel receiver with stratified two-phase flow regimen in transient states when solar irradiance is arriving on one side of receiver, Sol. Energy 76 (2004) 195–198.

Steven, G., Macosko, R.P., 1999. Transient thermal analysis of a refractive secondary solar collector. SAE Technical Paper, No. 99–01–2680.

M.F. Modest. Radiative heat transfer. 2nd ed. California: Academic Press; 2003.

R. Siegel, J.R. Howell. Thermal radiation heat transfer. 4th ed. New York/London: Taylor & Francis; 2002

Y. Shuai, X.L. Xia, H.P. Tan, Radiation performance of dish solar collector/cavity receiver systems, Sol. Energy 82 (2008) 13–21.

F.Q Wang, Y. Shuai, G. Yang, Y. Yuan, H.P Tan. Thermal stress analysis of eccentric tube receiver using concentrated solar radiation. Solar Energy, 2010, Accepted.

J.H. Fauple, F.E. Fisher, Engineering design–a synthesis of stress analysis and material engineering, Wiley, New York, 1981.

Y.F. Qin, M.S. Kuba, J.N. Naknishi, Coupled analysis of thermal flow and thermal stress of an engine exhaust manifold, SAE Technical Paper 2004-01-1345.
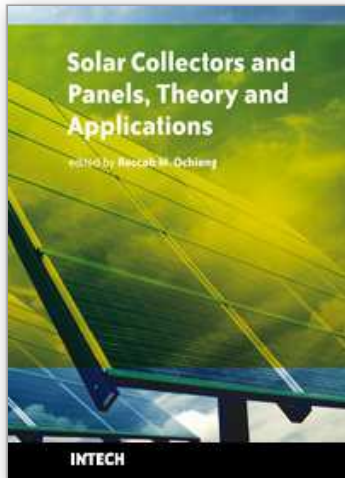
Solar Collectors and Panels, Theory and Applications

Edited by Dr. Reccab Manyala

This book provides a quick read for experts, researchers as well as novices in the field of solar collectors and panels research, technology, applications, theory and trends in research. It covers the use of solar panels applications in detail, ranging from lighting to use in solar vehicles.

How to reference

In order to correctly reference this scholarly work, feel free to copy and paste the following:

INTECH
open science | open minds